Synthetic Aperture Sequential Beamformation applied to medical imaging.

Hemmsen, Martin Christian; Hansen, Jens Munk; Jensen, Jørgen Arendt

Published in:
9th European Conference on Synthetic Aperture Radar

Publication date:
2012

Synthetic Aperture Sequential Beamformation applied to medical imaging.

Martin Christian Hemmsen, Jens Munk Hansen, and Joergen Arendt Jensen
Center for Fast Ultrasound Imaging, Department of Electrical Engineering,
Technical University of Denmark, DK-2800 Kgs. Lyngby, Denmark

Abstract

Synthetic Aperture Sequential Beamforming (SASB) is applied to medical ultrasound imaging using a multi element convex array transducer. The main motivation for SASB is to apply synthetic aperture techniques without the need for storing RF-data for a number of elements and hereby devise a system with a reduced system complexity. Using a 192 element, 3.5 MHz, λ-pitch transducer, it is demonstrated using tissue-phantom and wire-phantom measurements, how the speckle size and the detail resolution is improved compared to conventional imaging.

1 Introduction

In multi-element Synthetic Aperture (SA) imaging, the basic idea is to create a pressure wave from multiple elements with a focused transmission. The concept of using the transmit focal point as a virtual source was introduced by Passmann and Ermert [1]. Virtual sources in Synthetic Aperture Focusing (SAF) was further investigated by Frazier and O'Brien [2], Nikolov and Jensen [3, 4], and Bae and Jeong [5]. It was shown that the virtual source coincides with the focal point of the transducer, and that a depth independent resolution can be achieved. Kortbek et al. introduced [6] the concept of Sequential Beamforming to SA imaging to reduce system requirements for real time implementation. For a multi element linear array transducer, the lateral resolution can be made more range independent and improved significantly compared to conventional imaging using Dynamic Receive Focusing (DRF).

The basic idea in Synthetic Aperture Sequential Beamforming (SASB) is to create a dual-stage procedure using two separate beamformers. In the initial stage a beamformer using a single focal point in both transmit and receive, creates a set of focused scan lines. A second stage beamformer creates a set of high resolution image points by combining information from multiple first stage focused scan lines, which results in a dynamically expanding array as the image depth increases and a more range independent lateral resolution is obtained.

This paper evaluates the feasibility of applying SASB to medical ultrasound imaging using a multi element convex array transducer. The method is assessed and performance is quantized through a combination of water tank and tissue phantom measurements.

2 Method

SASB creates a set of N focused scan lines from M emissions using a first stage beamformer with a fixed receive time-delay profile. The delay profile is found from the round trip time-of-flight calculated as

$$t_d(\vec{r}_r) = \frac{1}{c}\Big(|\vec{r}_{tfp} - \vec{r}_e| \pm 2|\vec{r}_{fp} - \vec{r}_{tfp}| + |\vec{r}_r - \vec{r}_{tfp}|\Big). \quad (1)$$

The $\pm$ in (1) refer to whether the image point is above or below the transmit focal point. **Figure 1** illustrates the time-of-flight calculation for the SASB first stage beamformer.

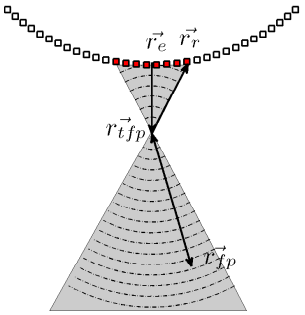

Figure 1: Wave propagation path (solid line) for calculating the receive focusing time delays for a fixed focused scan line.

Each point in the focused scan line contains information from a set of spatial positions limited by the opening angle, $\alpha = 2\arctan(1/(2F\#))$, of the virtual source. A single image point is therefore potentially represented in multiple first stage focused scan lines.
A second stage beamformer creates a set of high resolution image points by combining information from multiple first stage focused scan lines. A single sample, h, representing

the image point at location, $\vec{r}_{ip}$, is calculated as

$$h(\vec{r}_{ip}) = \sum_{k=1}^{N} \mathcal{W}(l_{\theta_k}, \vec{r}_{ip}) l_{\theta_k}(t_{d_k}(\vec{r}_{ip})), \quad (2)$$

where $l_{\theta_k}(t_{d_k}(\vec{r}_{ip}))$ is the sample at time t_{d_k} from the scan line, l, with propagation direction θ_k. The variable $\mathcal{W}$ is an apodization function with N values, which controls the weighting of the contribution from each of the N first stage scan lines. The time delay, t_{d_k} for the individual scan lines are found from the round trip time-of-flight,

$$t_{d_k}(\vec{r}_{ip}) = \frac{2}{c}\Big(|\vec{r}_{VS} - \vec{r}_{\theta_k}| \pm |\vec{r}_{ip} - \vec{r}_{VS}|\Big), \quad (3)$$

where $\vec{r}_{\theta_k}$ is the scan line reference position, and $\vec{r}_{VS}$ is the position of the virtual source. **Figure 2(a)** illustrates the time-of-flight calculation for the SASB second stage beamformer.

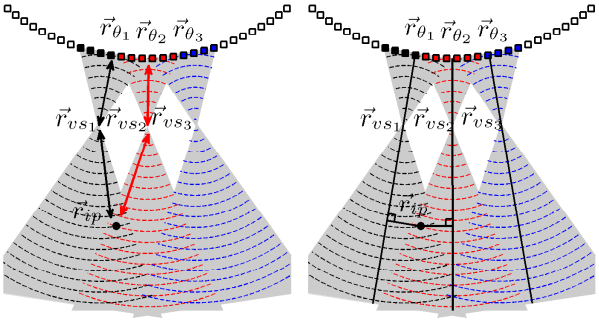

(a) Time-of-flight calculation (b) Apodization weight calculation

Figure 2: Visualization of (a) time-of-flight calculation and (b) apodization weight calculation.

The variable $\mathcal{W}$ in (2) is an apodization function determining the weighting of the individual scan lines. The weight for the scan line, l_{θ_k}, contributing to a specific image point can be calculated from (4)

$$\mathcal{W}(l_{\theta_k}, \vec{r}_{ip}) = \begin{cases} 0.54 + 0.46\cos(2n\pi), & \text{if } n \text{ is } \leq 1 \\ 0, & \text{if } n \text{ is } > 1 \end{cases} \quad (4)$$

for the case of a desired Hamming apodization, where n can be calculated from

$$n = \frac{d(l_{\theta_k}, \vec{r}_{ip})}{\Delta}, \quad (5)$$

and is given as the ratio between the shortest distance, $d(l_{\theta_k}, \vec{r}_{ip})$ from the image point to the scan line, and a desired aperture width, Δ. The distance $d(l_{\theta_k}, \vec{r}_{ip})$ can be expressed as

$$d(l_{\theta_k}, \vec{r}_{ip}) = \frac{\|(\vec{r}_{\theta_k} - \vec{r}_{VS_k}) \times (\vec{r}_{VS_k} - \vec{r}_{ip})\|}{\|\vec{r}_{\theta_k} - \vec{r}_{VS_k}\|} \quad (6)$$

where $\vec{r}_{\theta_k}$ is the reference point of the scan line. **Figure 2(b)** illustrates the apodization weight calculation.

2.1 Performance Indicators

Detail resolution The *detail resolution* is the separation at which identically point targets can be distinguished. It is distinguished by the main lobe width of the point-spread-function (PSF) and the 6 dB axial pulse length, i.e. the lateral and axial full width at half maximum (FWHM) of the PSF.

Cystic resolution The *cystic resolution* [7] is a measure that considers the ability to detect anechoic or weakly echogenic objects in the presence of strong surrounding objects, and can be quantized by the clutter energy to total energy ratio (CTR). The CTR is defined as the ratio of the energy outside a circular region $\Re$ with radius R centered at the peak of the PSF to the total PSF energy

$$\mathrm{CTR}_R(\vec{r}_0) = 10\log\left(1 - \frac{\int_{\vec{r}\in\Re} |h(\vec{r}, \vec{r}_0)|^2 dS}{\int |h(\vec{r}, \vec{r}_0)|^2 dS}\right),$$

where $|h(\vec{r}, \vec{r}_0)|$ is the PSF at $\vec{r}_0$. To get a single measure, one either measures the drop in brightness for a fixed radius R or the radius for which a cyst can be observed at a fixed level, e.g. $R_{12\mathrm{dB}} \equiv \{R \,|\, \mathrm{CTR}_R = 12\mathrm{dB}\}$.

Tissue contrast resolution The theoretical model proposed by Smith et al. [8] is a measure that considers the task of identifying a lesion within a uniform background for an ideal observer. The model states that the signal-to-noise ratio for lesion detection is

$$\mathrm{SNR}_{\Delta I} = \frac{C d N_{\mathrm{eff}}{}^{1/2}}{(S_{\mathrm{lat}} S_{\mathrm{ax}})^{1/2}},$$

where C is the contrast of a circular lesion of diameter d, S_{lat}, and S_{ax}, are, respectively, the lateral and axial speckle dimension, and N_{eff} is the number of independent images. To improve detectability of a lesion with a given contrast, it is therefore of great interest to maximize the density

$$\frac{N_{\mathrm{eff}}}{(S_{\mathrm{lat}} S_{\mathrm{ax}})}, \quad (7)$$

which will be refered to as the *speckle information density* (SID). The number of independent images, N_{eff} can be estimated by measuring the signal-to-noise ratio at a point, SNR_0 and using that the envelope-detected signals follow Rayleigh statistics [9]

$$N_{\mathrm{eff}} = \left(\frac{\mathrm{SNR}_0}{1.91}\right)^2. \quad (8)$$

The speckle dimensions, S_{lat} and S_{ax} can be found from the correlation cell

$$S_c = \int_{-\infty}^{\infty} \frac{C_I(\Delta\xi)}{C_I(0)} d(\Delta\xi), \quad (9)$$

where C_I is the spatial auto-covariance for the intensity and $\Delta\xi$ is the distance between image points.

3 Results

To investigate the performance of SASB, a setup using a commercial available 3.5 MHz, 192 element, λ-pitch convex array transducer (Sound Technology Inc., State College, PA, USA) was used for water tank and tissue phantom measurements. The data acquisition was done using a commercial available 2202 ProFocus ultrasound scanner (BK-Medical, Herlev, Denmark), capable of storing beamformed baseband data [10]. For SASB and DRF imaging, a sliding 63 element sub-aperture was used for 384 focused emissions respectively for SASB and DRF. Acquisitions were done interleaved and beamformed data were stored for off-line processing. For all emissions, a manufacturer default excitation pulse was used with no transmit apodization on the active sub-aperture. The emission for each sub-aperture was constructed using a fixed F-number corresponding to a focal depth of 69 mm. In receive SASB generated scan lines were created using a Gaussian receive apodization ($\alpha = 0.5$) applied to the same active sub-aperture as in transmit. DRF generated scan lines were created using a dynamic receive aperture maintaining a constant F-number of 0.8 and dynamic receive apodization using a Gaussian apodization ($\alpha = 0.5$).

3.1 Water phantom measurements

To evaluate the cystic resolution, and detail resolution a water tank phantom consisting of 4 wires at depths 16, 41, 66, and 91 mm were used. The transducer was submerged into the water and data were collected. **Figure 3** illustrates the measured PSF at depths of 41 and 91 mm as 6 dB contour plots with a dynamic range of 60 dB.

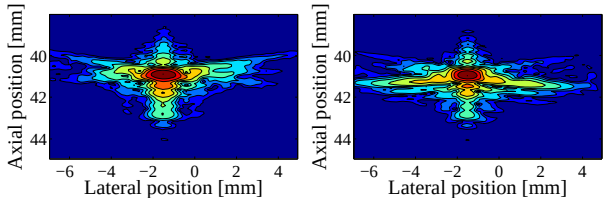

(a) PSF using DRF at 41 mm (b) PSF using SASB at 41 mm

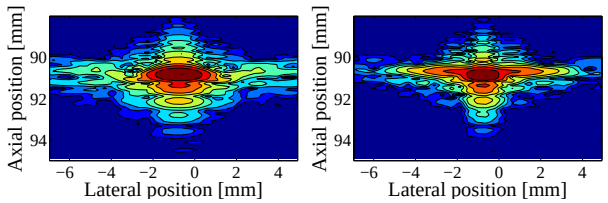

(c) PSF using DRF at 91 mm (d) PSF using SASB at 91 mm

Figure 3: Measured PSF at depths of 41 and 91 mm obtained using a water tank phantom. The figures (a+c) is made using DRF and (b+d) using SASB.

Comparing the contours, the PSF using SASB is less range dependent and has an improved lateral resolution in terms of the FWHM. The improvement in FWHM comes at a cost in side-lobe level. The near side-lobes are higher using SASB, they do however fall off faster than using DRF.

Table 1: Contrast resolution, FWHM, and detail resolution extracted from the water tank measurements.

	$R_{12\text{dB}}$ [mm]	FWHM_{lat} [mm]	FWHM_{ax} [mm]	$\text{Area}_{6\text{dB}}$ [mm^2]
$\text{DRF}_{41\text{mm}}$	0.51	0.79	0.41	0.26
$\text{SASB}_{41\text{mm}}$	0.46	0.71	0.41	0.23
$\text{DRF}_{91\text{mm}}$	1.25	2.29	0.64	1.15
$\text{SASB}_{91\text{mm}}$	1.69	1.54	0.56	0.68

From the results in **Table 1** it follows that the axial and lateral resolution at FWHM is improved using SASB. The axial and lateral resolution at FWHM is respectively in average improved by 3% and 22%. The cystic resolution at 12 dB is improved at 41 mm, but is degraded at 91 mm. The degradation at 91 mm is due to the high near side-lobe level. **Figure 4** illustrates the CTR together with the clutter level for the two wires. Note that the CTR for the SASB images are in general equally good or better for any radius, but for radius between 1 and 4 mm. The clutter level is improved using SASB for any radius.

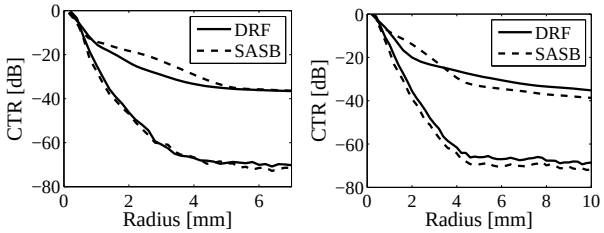

(a) CTR at 41 mm (b) CTR at 91 mm

Figure 4: CTR for dynamic receive focusing (thick solid lines) and synthetic aperture sequential beamforming (thick dashed lines). Clutter levels are shown below as thin dashed and solid lines.

3.2 Tissue phantom measurements

To investigate the performance for lesion detection, a tissue mimicking phantom was scanned and speckle size, and SNR_0 were calculated for 20x20 mm regions at depths ranging from 20 to 140 mm. **Table 2**, shows the result for the two regions with centers at 41 and 91 mm. From the figure it follows that the speckle size is on average reduced by 15.3%, and the speckle information density is improved by 12% using SASB. **Figure 5(a)** illustrates the speckle size and speckle information density in the range from 20 to 140 mm. **Figure 6** illustrates two regions from the tissue phantom with small anechoic objects for a visual comparison of the tissue contrast resolution.

Table 2: Signal-to-noise ratio at a point, SNR_0, speckle size and the density $N_{\mathrm{eff}}/(S_{\mathrm{ax}}S_{\mathrm{lat}})$.

	SNR_0	Speckle size [mm^2]	$N_{\mathrm{eff}}/(S_{\mathrm{ax}}S_{\mathrm{lat}})$ [mm^{-2}]
$\mathrm{DRF}_{41\mathrm{mm}}$	1.87	0.32	2.37
$\mathrm{SASB}_{41\mathrm{mm}}$	1.86	0.27	2.73
$\mathrm{DRF}_{91\mathrm{mm}}$	1.85	0.54	1.37
$\mathrm{SASB}_{91\mathrm{mm}}$	1.87	0.46	1.63

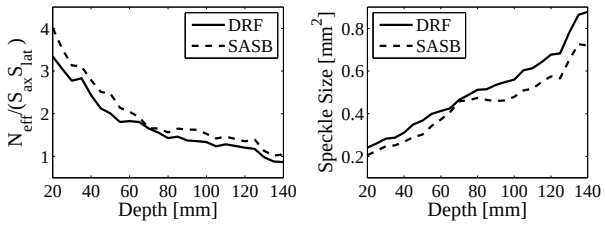

(a) Speckle Information Density (b) Speckle size

Figure 5: Visualization of (a) speckle information density and (b) speckle size calculated from the tissue phantom measurement, using SASB (dashed line) and DRF (solid line).

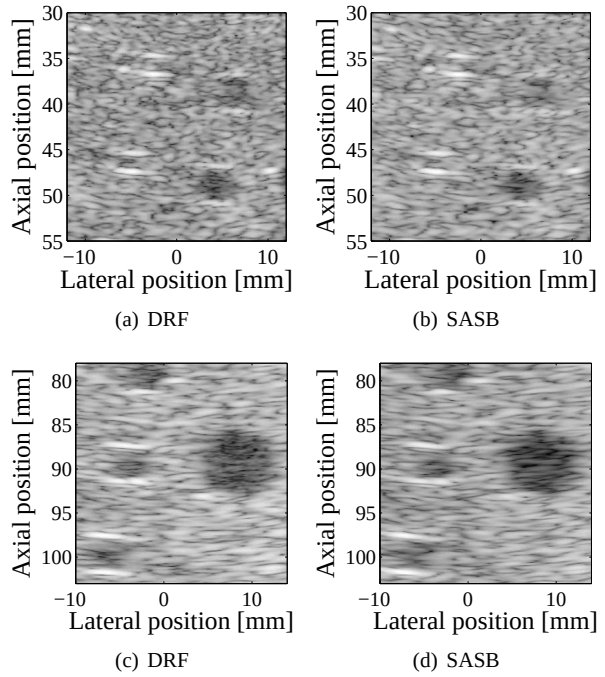

(a) DRF (b) SASB

(c) DRF (d) SASB

Figure 6: B-mode images of the tissue phantom with small anechoic objects (a+c) using DRF and (b+d) using SASB.

4 Conclusion

SASB has been successfully implemented for a convex multi element array transducer. Evaluation using water and tissue phantom measurements indicate a performance improvement for detail resolution, speckle size, and speckle information density. The evaluation show that SASB is able to increase the image range of a uniform lateral resolution and to obtain a more isotropic point spread function. The results presented in this paper proves the viability of the method for real-time 2D ultrasound imaging using commercially available equipment.

References

[1] C. Passmann and H. Ermert, *A 100-MHz ultrasound imaging system for dermatologic and ophthalmologic diagnostics*, IEEE Trans. Ultrason., Ferroelec., Freq. Contr., vol. 43, pp. 545–552, 1996

[2] C. H. Frazier and W. D. O'Brien, *Synthetic aperture techniques with a virtual source element*, IEEE Trans. Ultrason., Ferroelec., Freq. Contr., vol. 45, pp. 196–207, 1998

[3] S. I. Nikolov and J. A. Jensen, *Virtual ultrasound sources in high-resolution ultrasound imaging*, in Proc. SPIE - Progress in biomedical optics and imaging, vol. 3, pp. 395–405, 2002

[4] ——, *3D synthetic aperture imaging using a virtual source element in the elevation plane*, in Proc. IEEE Ultrason. Symp., vol. 2, pp. 1743–1747, 2000

[5] M. H. Bae and M. K. Jeong, *A study of synthetic-aperture imaging with virtual source elements in B-mode ultrasound imaging systems*, in IEEE Trans. Ultrason., Ferroelec., Freq. Contr., vol. 47, pp. 1510–1519, 2000

[6] J. Kortbek, J. A. Jensen, and K. L. Gammelmark, *Synthetic aperture sequential beamforming*, Ultrasonics, p. Submitted, 2009

[7] D. Vilkomerson, J. Greenleaf, and V. Dutt, *Towards a Resolution Metric for Medical Ultrasound Imaging*, in Proc. IEEE Ultrason. Symp., pp. 1405–1410, 1995

[8] S. W. Smith, R. F. Wagner, J. M. Sandrik, and H. Lopez, *Low contrast detectability and contrast/detail analysis in medical ultrasound*, Ultrason. Imaging, vol. 30, no. 3, pp. 164–173, May 1983

[9] R. F. Wagner, S. W. Smith, J. M. Sandrick, and H. Lopez, *Statistics of speckle in ultrasound B-scans*, IEEE Trans. Son. Ultrason., vol. 30, pp. 156–163, 1983

[10] M. C. Hemmsen, S. I. Nikolov, M. M. Pedersen, M. J. Pihl, M. S. Enevoldsen, J. M. Hansen, and J. A. Jensen, *Implementation of a versatile research data acquisition system using a commercially available medical ultrasound scanner*, IEEE Trans. Ultrason., Ferroelec., Freq. Contr., p. Accepted, 2011